Pergamon

Int. J. Heat Mass Transfer. Vol. 41, Nos 8–9, pp. 979–991, 1998

Printed in Great Britain
0017-9310/98 $19.00+0.00

PII: S0017-9310(97)00225-1

Three-dimensional mixed convection in a rotating multiple-pass square channel

J. J. HWANG[1] and D. Y. LAI[2]

Institute of Aeronautical and Astronautics, Chung-Hua University, Hsinchu, Taiwan 300, R.O.C.

(*Received* 27 *September* 1996 *and in final form* 1 *August* 1997)

Abstract—A numerical study of three-dimensional mixed convection for a constant-property fluid flowing laminarly through a periodical two-pass square channel with radial rotation is presented. Thermal and fluid-flow fields are calculated for the entire domain from the Navier–Stokes equations and the energy equation by a finite-difference technique. The emphasis is placed on the rotating effects, including both the Coriolis force, and centrifugal buoyancy, on heat transfer in channels of different flow directions. Typical developments of the axial velocity, secondary flow, and fluid temperature are presented to illustrate in detail the influence of rotation on the heat transfer. The results reveal that, in a buoyancy-affected rotating two-pass channel, the local heat transfer is dependent on the flow direction, and the Coriolis-force effect is more notable for the radially inward flow than that for the radially outward flow. It is further found that the centrifugal buoyancy enhances significantly the peripherally averaged heat transfer in the radially inward-flow channel, but relatively negligibly in the radially outward-flow channel, which is analogous to the buoyancy-dependence of the cross-flow-intensity development. The prediction further demonstrates that, as long as the centrifugal buoyancy is sufficiently strong, the radially outward flow will separate from the leading surface, which largely deteriorates the wall heat transfer. A comparison of the present prediction with available numerical and experimental data for stationary and rotating ducts is also presented. © 1997 Elsevier Science Ltd.

INTRODUCTION

Heat transfer in rotating passages has attracted much attention of researchers because of their wide application in a variety of rotary machinery such as cooling in electrical machinery, rotor blades of turbine engines, and other rotating thermal systems. An example of internal cooling of rotor blades, which is closely related to the present study, is cited below. This method is to route coolant air through internal passages within the rotor blades to convectively remove heat from the blade that, in turn, protects the blades from a high-temperature environment. The cooling passages are usually cast into a serpentine channel that comprises several passages aligned with the blade spanwise direction and is connected by a 180° bend between any two adjacent passages. The thermal behavior within such passages is influenced by several factors, such as the presence of sharp 180° bends [1, 2] and sometimes the use of ribs for enhancing the heat transfer [3, 4]. The effects of rotationally induced Coriolis force are nevertheless of primary importance [5–12]. Moreover, in a high rotation speed and/or a high wall-to-coolant temperature difference, the centrifugal-buoyancy forces may play a very critical role in the heat transfer mechanisms [13–17]. The ability to predict how wall heat transfer is affected by rotation in multiple-pass channels, even with a simple wall geometry, is thus highly valuable to the designer of aero-engines. Although, the above-mentioned application would be turbulent flows, the present analysis addresses the laminar case which is relevant in some applications [5, 7] and is also of fundamental interest.

A large amount of research effort, both theoretical and experimental, has been conducted for flow and heat transfer characteristics in rotating channels. In earlier works of adiabatic rotating channel flows [5–8], the effect of the Coriolis force on the flow structure has been examined theoretically and experimentally, and the presence of secondary flow due to Coriolis forces has been well documented. Developing and/or fully developed forced convection in rotating heated channels has been carried out by [9–11]; however, these investigations do not consider the buoyancy effects induced by centrifugal force. Recently, many studies have been devoted towards the centrifugal-buoyancy effects on the fluid flow and heat transfer characteristics in radially rotating channels [12–17]. Except for some experimental efforts [15–17], most of the numerical investigations have dealt with only the heat transfer in a single-pass straight channel with radial rotation. Strictly speaking, prediction on mixed convection from the surfaces of radially rotating multiple-pass channels in view of the local heat transfer and flow structure has not been reported yet. This motivates the present study to predict the fluid flow and heat transfer in a multiple-pass square channel with radially rotating conditions. The emphasis of this

[1] Associate Professor, Phone: 886-35374281 Ext. 8334, Fax: 88635373771, E-mail: jjhwang@chu.edu.tw
[2] Graduate student.

NOMENCLATURE

AR ratio of the total heat transfer surface area of the module and channel cross sectional area
c_p specific heat at constant pressure [kJ kg^{-1} K^{-1}]
De channel hydraulic diameter or channel height (in Y direction) [m]
Gr Grashof number, $(\Omega^2 \cdot De) \cdot \beta_T \cdot q_w \cdot De^4/(v^2 \cdot k_f)$
h heat transfer coefficient [W m^{-2} K^{-1}]
k_f air thermal conductivity [W m^{-1} K^{-1}]
L_x module length (in X direction), i.e., $20De$ [m]
L_y module height (in Y direction), i.e., De [m]
L_z module width (in Z direction), i.e., $3De$ [m]
$\dot{m}$ mass flow rate [kg s^{-1}]
Nu_x single wall (spanwise) averaged Nusselt number
$\overline{Nu}$ channel averaged Nusselt number
$\overline{Nu}_x$ peripherally (four-wall) averaged Nusselt number
P, p dimensionless and dimensional cross sectional mean pressure
Pr Prandtl number
Q total heat input into a module [W]
q_w wall heat transfer [W m^{-2}]
Re Reynolds number, $\bar{W} \cdot De/v$
Re_Ω Rotational Reynolds number, $\Omega \cdot De^2/v$
Ro Rotation number, $\Omega \cdot De/\bar{W}$
T temperature of air [K]
T_b local bulk mean temperature of air [K]
T_r reference temperature [K]
T_w local wall temperature [K]
U, V, W dimensionless local velocity components in X, Y and Z directions, respectively.
$\bar{W}$ average streamwise velocity in the channel [m s^{-1}]
u, v, w local velocity components in X, Y, and Z directions, respectively [m s^{-1}]
X, Y, Z dimensionless rectangular coordinate, see Fig. 1
x, y, z rectangular coordinate [m].

Greek symbols
β pressure drop parameter [kPa m^{-1}]
β_T thermal expansion coefficient [K^{-1}]
σ averaged cross-flow intensity, $\int_0^{De}\int_0^{De} [(\sqrt{V^2+W^2})/\bar{W}]\,dY\,dZ/De^2$
γ air enthalpy rise parameter, $Q/(\dot{m} \cdot c_p \cdot L_z)$ [K m^{-1}]
θ dimensionless temperature
v kinematic viscosity [m^2 s^{-1}]
ρ air density [kg m^{-3}]
Ω angular velocity of rotation [s^{-1}].

Subscripts
b bulk mean
r reference
s smooth or stationary
w wall
x x-coordinate dependence.

Superscripts
* periodicity
average.

prediction is, of course, placed on the rotation effect, including the Coriolis and centrifugal-buoyancy forces, on the heat transfer in channels of different radial flow directions. It has been experimentally verified that the periodicity of local heat transfer along a rotating serpentine-type passage is achieved after the first turn of this channel [17]. That is the fully developed condition starts from the second-pass straight (radially inward) channel of the multiple-pass passage. Therefore, the multiple-pass channel can be readily simulated as a straight entrance channel followed by a number of periodic two-pass channels. Here, we focus our attention on a periodically fully developed situation, in which the flow and heat transfer characteristics are assumed to repeat themselves cyclically from the entrance of the two-pass channel to the next. This assumption allows the calculation domain to be limited to the region across a two-pass (inward plus outward) channel, as given in Fig. 1. It is believed that a substantial body of numerical/experimental data is highly required to accurately predict the heat transfer coefficient and flow field in this important area of rotary machinery. Moreover, the present numerical simulation may be helpful in the interpretation of the experimental results with unavoidable measuring errors.

THEORETICAL ANALYSIS

Figure 1 shows a physical configuration of the periodic two-pass channel, which consists of a radial-inward channel associated with a 90° miter entrance, a 180° sharp turn, and a radial-outward square channel associated with another 90° miter exit. The flow and

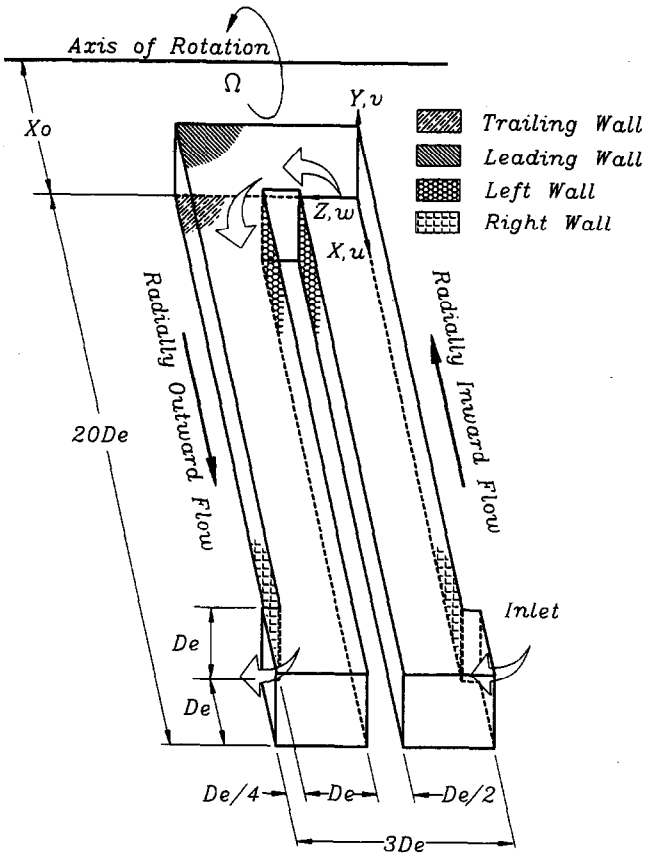

Fig. 1. Sketch of configuration, dimension, and coordinate system of the periodic two-pass module.

heat transfer characteristics at the entrance and exit of this periodic module should be identical via a suitable parameter reduction. The two-pass channel rotates at a constant angular speed Ω about the axis normal to the main flow direction (X). The u, v, and w are the velocity components of the X, Y, and Z directions. The labeling order of each wall of this two-pass channel is also given in Fig. 1. The orientation of "left" and "right" is chosen as one follows the main-stream direction passing through entire passage. Note also that both the trailing and leading walls in the radially inward and outward flow channels, respectively, will be referred as the low-pressure surfaces in the following discussion. In the same way, the high-pressure surfaces represent both the leading wall of the radially inward-flow channel and the trailing wall of the radially outward-flow channel. To facilitate the analysis, the flow is assumed to be steady and with constant properties, and the axial diffusion, viscous dissipation, and compression work are all ignored. In addition, gravitational inertia is neglected due to its small magnitude compared to the rotationally induced centrifugal force. The Boussinesq approximation of a linear density-temperature relation, i.e., $\Delta\rho/\rho = \beta_T(\Delta T)$, is quoted for the consideration of the centrifugal buoyancy. Since the centrifugal buoyancy is taken into consideration, the distance from the axis of rotation to the test module is very relevant, which is fixed at $X_0 = 10$ in the present study.

A comprehensive discussion of the periodically fully developed analysis is given by Patankar *et al.* [18], and all details are not elaborated on here. Basically, all flow variables repeat cyclically over the length of the computational module. The present test section can be regarded as a "periodically varied cross-section area" module in z direction; therefore, the physical quantities are decomposed in z direction. That is,

$$\varphi(x,y,z) = \varphi(x,y,z+3De) \tag{1}$$

where φ could be any velocity component (u, v, w). As for the pressure and temperature, they can be respectively decomposed as

$$p(x,y,z) = -\beta z + p^*(x,y,z) \tag{2}$$

$$T(x,y,z) = \gamma z + T^*(x,y,z) \tag{3}$$

where both the global pressure drop parameter $\beta = [p(x,y,z) - p(x,y,z+L_z)]/L_z$ and the temperature increase parameter $\gamma = [T(x,y,z+L_z) - T(x,y,z)]/L_z$ are constants. The functions p^*, and T^* identically repeat themselves from module to module. The terms $-\beta z$ and γz are, respectively, related to the general decrease and increase in pressure and fluid enthalpy along the module width direction (z). Practically, in

the periodic analysis, the flow rate is not known *a priori*. Solution for a given flow rate is achieved by iteratively updating the value of the global pressure gradient parameter β, until convergence is reached. That is for a given value of β, there will be a corresponding flow rate in the channel. The fluid enthalpy rise parameter, γ, can be expressed as the form $\gamma = Q/(\dot{m} \cdot c_p \cdot L_z)$ where Q is the total heat input over the module, $\dot{m}$ the mass flow rate, and c_p the specific heat. The dimensionless governing equations are:

Continuity:

$$\frac{\partial U}{\partial X} + \frac{\partial V}{\partial Y} + \frac{\partial W}{\partial Z} = 0 \tag{4}$$

x-momentum:

$$U\frac{\partial U}{\partial X} + V\frac{\partial U}{\partial Y} + W\frac{\partial U}{\partial Z} = -\frac{\partial P}{\partial X} + \frac{1}{Re}\left(\frac{\partial^2 U}{\partial X^2} + \frac{\partial^2 U}{\partial Y^2} + \frac{\partial^2 U}{\partial Z^2}\right) + 2RoV - \frac{Gr}{Re^2}\theta(X+X_0) \tag{5}$$

y-momentum:

$$U\frac{\partial V}{\partial X} + V\frac{\partial V}{\partial Y} + W\frac{\partial V}{\partial Z} = -\frac{\partial P}{\partial Y} + \frac{1}{Re}\left(\frac{\partial^2 V}{\partial X^2} + \frac{\partial^2 V}{\partial Y^2} + \frac{\partial^2 V}{\partial Z^2}\right) - 2RoU - \frac{Gr}{Re^2}\theta Y \tag{6}$$

z-momentum:

$$U\frac{\partial W}{\partial X} + V\frac{\partial W}{\partial Y} + W\frac{\partial W}{\partial Z} = -\frac{\partial P}{\partial Z} + \frac{1}{Re}\left(\frac{\partial^2 W}{\partial X^2} + \frac{\partial^2 W}{\partial Y^2} + \frac{\partial^2 W}{\partial Z^2}\right) - \beta' \tag{7}$$

Energy:

$$U\frac{\partial \theta}{\partial X} + V\frac{\partial \theta}{\partial Y} + W\frac{\partial \theta}{\partial Z} = \frac{1}{RePr} \times \left(\frac{\partial^2 \theta}{\partial X^2} + \frac{\partial^2 \theta}{\partial Y^2} + \frac{\partial^2 \theta}{\partial Z^2}\right) - \gamma' W \tag{8}$$

where $Re = \bar{W} De/\nu$, $Ro = Re_\Omega/Re$, $Re_\Omega = \Omega\ De^2/\nu$, and $Gr = (\Omega^2 \cdot De) \cdot \beta_T \cdot q_w \cdot De^4/(\nu^2 \cdot k_f)$. The other dimensionless variables chosen are:

$$X = x/De, \quad Y = y/De, \quad Z = z/De,$$

$$U = u/\bar{W}, \quad V = v/\bar{W}, \quad W = w/\bar{W}, \quad P = p^*/(\rho \cdot \bar{W}^2),$$

$$\beta' = \beta \cdot De/(\rho \cdot \bar{W}^2), \quad \theta = k_f \cdot (T^* - T_r)/(q_w \cdot De),$$

$$\gamma' = \gamma/(q_w/k_f) = AR \cdot De/(L_z \cdot Re \cdot Pr) = AR/(2Re \cdot Pr)$$

Note that the dimensionless fluid enthalpy rise parameter γ' is independent of the quantity of the wall heat flux q_w which affects the thermal-fluid fields by changing the magnitude of Gr. The terms $2RoV$ and $2RoU$ on the right hand side of eqns (5) and (6) are the Coriolis force driving the flow in the X and Y directions, respectively. The centrifugal buoyancy forces in eqns (5) and (6), $(Gr/Re^2)\,\theta(X+X_0)$ and $(Gr/Re^2)\,\theta Y$, are non-uniformly distributed on the YZ and XW planes, respectively, due to the variation of the temperature distribution.

The boundary conditions of this problem can be expressed as:

(1) Channel wall

$$U = V = W = 0, \quad \partial\theta/\partial n = 1$$

(2) Periodic conditions at the channel inlet and outlet

$$U(X, Y, Z) = U(X, Y, Z+3),$$
$$V(X, Y, Z) = V(X, Y, Z+3)$$
$$W(X, Y, Z) = W(X, Y, Z+3),$$
$$\theta(X, Y, Z) = \theta(X, Y, Z+3)$$

Investigated parameters

After the velocity and temperature fields of the full-domain are obtained, the computations of the local and peripherally-averaged Nusselt numbers are of practical interest. Following the conventional definitions, the local Nusselt number of the channel wall is defined as follows:

$$Nu = h \cdot De/k_f = q_w \cdot De/[k_f \cdot (T_w - T_b)] = 1/\theta_w \tag{9}$$

where q_w is the local heat transfer rate from the channel wall, and T_w the local wall temperature of the channel. The local bulk mean temperature T_b is determined as

$$T_b = \int T|U|\,dA \Big/ \int |U|\,dA \tag{10}$$

where the integrals are to be carried over the cross-sectional area of the channel. The absolute value of the velocity is taken so that the regions with the reverse flows are also properly represented.

The investigated parameters for the present study are the rotation number, $Ro = 0$–0.5, and the rotating buoyancy force, $Gr = 0$–$50{,}000$.

Computational details

The solving procedure developed in this work is based on the finite-volume discretization of eqns (4)–(7) [19]. this procedure ensures conservation of mass, momentum, and energy over each control volume. Velocity control volumes are staggered with respect to the main control volumes, and coupling of the pressure and velocity fields is treated via the SIMPLER [20] pressure correction algorithm. In order to reduce numerical diffusion resulting from the exis-

tence of large cross-flow gradients and obliquity of the flow to the grid lines, the smooth hybrid central/skew upstream difference scheme (SCSUDS) is used for the diffusion and convective terms, which has been described in detail in Liou *et al.* [21]. The set of the differential equations over the entire region of interest is solved by obtaining new values for any desired variables, taking into account the latest known estimated values of the variable from the neighboring nodes. One iteration process is complete when, in line-by-line technique, all lines in a direction have been accounted for. Because of the large variations in the source terms, under-relaxation is necessary for the dependent variables and the source terms to achieve convergence. Line inversion iteration with typical under-relaxation values of 0.5 for the velocity terms and 0.7 for the pressure correction term are incorporated to the facilitated calculation. Solutions are considered to be converged at each test condition after the ratio of residual source (including mass, momentum, and energy) to the maximum flux across a control surface is below 1.0×10^{-3}.

Grid refinement

In this problem, most of the real action is found around the 180° turns and near all solid surfaces and, therefore, nodes are clustered in these regions in order to resolve the strong gradients present there. All computations are performed on $72 \times 20 \times 50$ (X, Y, Z) grids in the present work. Additional runs for the coarser meshes, $50 \times 15 \times 40$, and the finer meshes, $90 \times 30 \times 70$, are taken for a check of grid independence. The parameters used to check the grid independence are axial velocity profile, temperature profile, and the local Nusselt number distribution. A comparison of the results of the two grid sizes, $72 \times 20 \times 50$ and $90 \times 30 \times 70$, shows that the maximum discrepancies in the axial velocity and temperature profiles are 0.9 and 1.5%, respectively, for the stationary condition ($Re_\Omega = 0$). Computations for $Re_\Omega = 500$ are also conducted and the results indicate a maximum change of 2.2% in Nusselt number distribution between the solutions of $72 \times 20 \times 50$, and $90 \times 30 \times 70$ grids. These changes are so small that the accuracy of the solutions on a $72 \times 20 \times 50$ grids is deemed satisfactory.

Numerical computation of the periodically fully developed flow is rendered difficult by the fact that no boundary information is available in the main flow direction along which the discretization coefficients are largest. Partly due to this reason, the code takes as high as 5000–6000 iterations for convergence. On Convex-C3840, this translated to about 150 min of CPU time.

PRESENTATION OF RESULTS

Although, significant heat transfer enhancements in the region of the 180° turn are anticipated, due to the space limitation, the present presentation focuses on the examination of the effect of rotation on heat transfer in straight channels of different flow directions, i.e. the radial-inward and radial-outward flow channels.

Prior to discussing the computational results, it is necessary to validate present numerical procedure and data by comparing the present results with those in previous works. Since the experimental fluid-field data are not available for flow over rotating two-pass channels up to now, the present calculations are compared with those in a stationary two-pass channel [1]. Figure 2(a) is a smoke-injection visualization of flow patterns on the YZ plane cutting across the axial station $X = 0.25$ (i.e., in the sharp turn region). The present numerical results for the secondary-flow vectors and main-flow contours at this station are given in Fig. 2(b) and (c), respectively, with slight difference in the Reynolds number. It is seen that both the experimental and simulated results reveal that two vortices exist around two upper concave corners of the channel. Moreover, the dense-smoke (bright) region in the visualized photo is coincident with the region of low main-flow velocity as given in Fig. 2(c). This is very reasonable because the region of lower main-flow velocity could keep the smoke, and in the higher main-flow velocity region the smoke is easily blown off. Hence, the dark region is found in the central portion of the channel as given in Fig. 2(a). The comparison above confirms that the present numerical procedure is adequate and the present numerical results are reliable.

Evolution of cross-flows

Figure 3 gives the typical results of the secondary-flow evolution along the streamwise direction in a rotating two-pass square channel with various rotating buoyancy. The Reynolds number and the rotation number are fixed at $Re = 1000$, and $Ro = 0.1$, respectively. In the buoyancy-free case, as shown in Fig. 3(a), the secondary flow patterns are rather complex at the station near the inward straight channel entrance, $X = 17.8$, due to the centrifugal inertia caused by flow curvature in the upstream 180° sharp turn, rotation induced Coriolis force, and their interaction. As the flow moves downstream, the centrifugal-inertial effect gradually lays off, and the coriolis-force effect becomes important. It is seen that at the station $X = 10$, the well-known counter-rotating vortex pair caused by Coriolis force, which circulates from the leading to the trailing walls along the two side walls and returns back through the central core of the flow, has been well established. A slight imbalance of these two counter-rotating vortices is because of the non-uniform inlet condition caused by the upstream 180° sharp turn. As the flow further goes downstream to $X = 2.2$, the counter-rotating vortices are slightly weaker because the fluid feels the downstream sharp turn. When the flow has turned around the 180° sharp bend into the radially outward straight channel, regardless the flow direction, the secondary-flow patterns are largely identical to those in the radi-

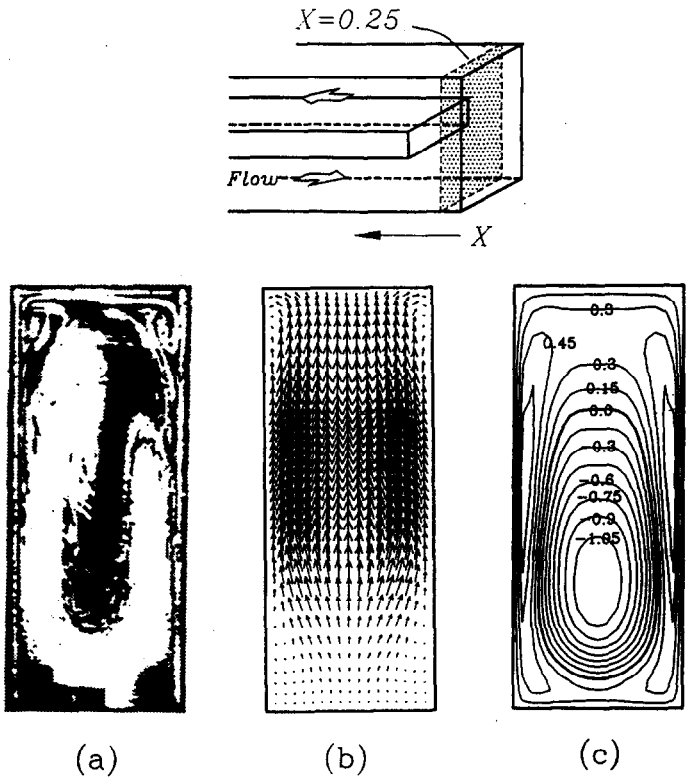

Fig. 2. Comparison of the present numerical results with the previous flow visualization results, (a) smoke-injection visualization, $Re = 200$, $Ro = 0$ [1], (b) secondary-flow vectors, and (c) iso-speed contours of the main flow, $Re = 300$, $Ro = 0$.

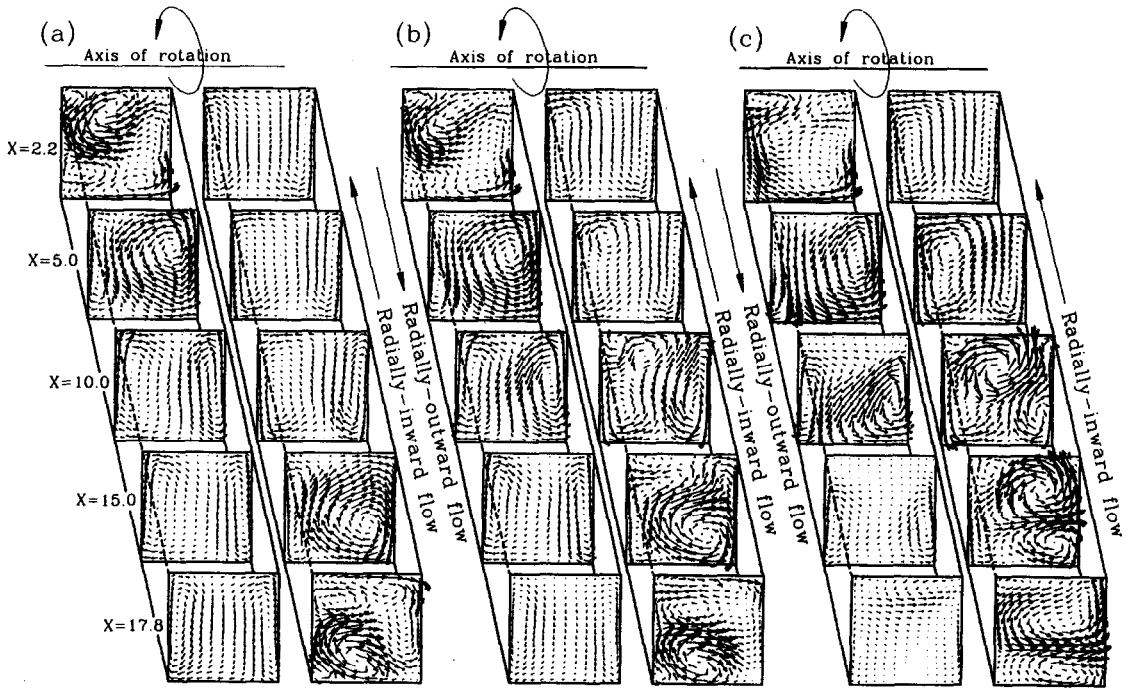

Fig. 3. Development of the cross flow $(V+W)$ along the axial distance of the two-pass channel, (a) $Gr = 0$, $Ro = 0.1$, and $Re = 1000$, (b) $Gr = 10{,}000$, $Ro = 0.1$ and $Re = 1000$, (c) $Gr = 50{,}000$, $Ro = 0.1$ and $Re = 1000$.

ally inward-flow channel at the corresponding stations of the same distance relative to the sharp turn. This is very reasonable because the rotationally induced buoyancy is neglected and, therefore, only the opposite direction of the Coriolis force acting on these two channels, which is directed at the trailing wall and leading wall for the radially outward-flow channel and radially inward-flow channel, respectively.

When the rotating buoyancy force acts on this two-pass channel, as expected, the evolution of the secondary flow is never to be the same between the radial-inward-flow channel and radial-outward-flow channel due to the different mechanisms of the interaction between the rotating induced buoyancy and Coriolis forces. In the radially inward-flow channel, the rotating induced buoyancy directs downstream of the main flow; whereas it is in direction against the main flow in the radially outward-flow channel. It is observed from Fig. 3(b), in the radially inward flow channel with the lower buoyancy ($Gr = 10{,}000$), the counter-rotating vortex pair at the station $X = 10$ and downstream is evidently distorted. An additional vortex-pair is bifurcated around the corner formed by the leading and left walls. This phenomenon is, however, not found at the corresponding station for the radially outward-flow channel. When the centrifugal buoyancy is further increased to $Gr = 50{,}000$, as given in Fig. 3(c), the secondary-flow structure seems to be more complex in the radially inward-flow channel. On the other hand, in the radially outward-flow channel, the Coriolis-induced vortex-pair is significantly deflected to the trailing wall, e.g., at the station $X = 10$. A relatively stagnant cross-flow velocity is further found near the leading wall, which is because the flow reversal happens near this wall region and will be shown by the main flow velocity profiles later. It is concluded from this figure that, relatively, the centrifugal-buoyancy effect in the radially inward-flow channel enhances the strength of the cross-flow, but insignificantly in the radially outward-flow channel. Additional quantitative outcomes will be shown later by comparing the cross-flow-intensity distributions between the channels of different flow directions.

Axial velocity profiles

The axial-velocity profiles across the straight-channel-centerlines ($Z = 0.5$, and 2.0) between the high- and low-pressure surfaces of the two-pass channel at some selected axial locations with different rotating buoyancy forces are shown in Fig. 4. The letters L and T on this graph respectively denote the leading and trailing walls. It is shown that the buoyancy-free channel (solid curve) has exactly alike axial-velocity profiles between the radially inward-flow and outward-flow channels if the axial distance relative to the upstream sharp turn is the same. By taking the buoyancy force into consideration, we can find that the axial velocity has got out of shape. The magnitude of axial velocity near the trailing wall for both the radially inward-flow and outward-flow channels is found to be larger than the buoyancy-free case (excluding the stations near the straight channel entrance), and increases with an increase of Gr. The former is because, in the radially inward-flow channel, the centrifugal buoyancy is coincident with the main-flow direction, which favors the relatively hot fluid near the trailing wall and, hence, accelerates the fluid near the trailing wall. In the radially outward-flow channel, however, the centrifugal buoyancy directs against to the main flow, which is greater on the fluid near the leading wall (relatively warm) and smaller on the fluid near the trailing wall (relatively cool); consequently, due to the imbalance of the force, the radial velocity of the fluid decreases near the leading wall and increases near the trailing wall. Note that, if the heat input to the coolant is sufficiently large, say $Gr = 50{,}000$, the deceleration in axial velocity near the leading wall of the radially outward-flow channel results in the flow separation from the wall, and then the flow goes upstream over the leading wall. General tendency observed in this figure is that the centrifugal-buoyancy effect is disposed to flatten the axial-velocity curves of the radially inward-flow channel, and to sharpen those of the radially outward-flow channel.

Temperature contours

The axial variations of isothermal contours in the present two-pass channel at several different centrifugal-buoyancy conditions are given in Fig. 5. Basically, the strength of the thermal-field distribution is in contrast to that in the fluid-flow field. The region of high velocity where most heat is convected away by the fluid, is the region of lower temperature. In the buoyancy-free case (Fig. 5(a)), near the straight-channel entrance ($X = 17.8$, and 2.2 for the radially inward-flow and outward-flow channels, respectively), the relatively low temperature cores ($\theta = 0.04$, and 0.16, respectively) are found to be in the region near the left and right walls for the radially inward and outward flow channels, respectively. This is attributed to the strong washing-effect by curved flow turning around the sharp bend. As flow marches downstream, the Coriolis-force effect is gradually increased, which subsequently forces the cold-fluid core in direction of the leading wall and trailing wall for the radially inward-flow and outward-flow channels, respectively. Note that after five channel hydraulic diameters of the sharp-turn downstream, the wall temperature on the low-pressure surface has been significantly higher than that on the high-pressure surfaces. This implies a lower heat transfer on the lower-pressure surface as compared with that on the higher-pressure surface. Comparing Fig. 5(a) and (c) reveals that the fluid temperature distributions in the buoyancy-assisted flowing channel are more uniform than those in the buoyancy-free channel at the corresponding station, which are subsequently more uniform than those in the buoyancy-against flowing channel. It is highly noted from Fig. 5(c) that sub-

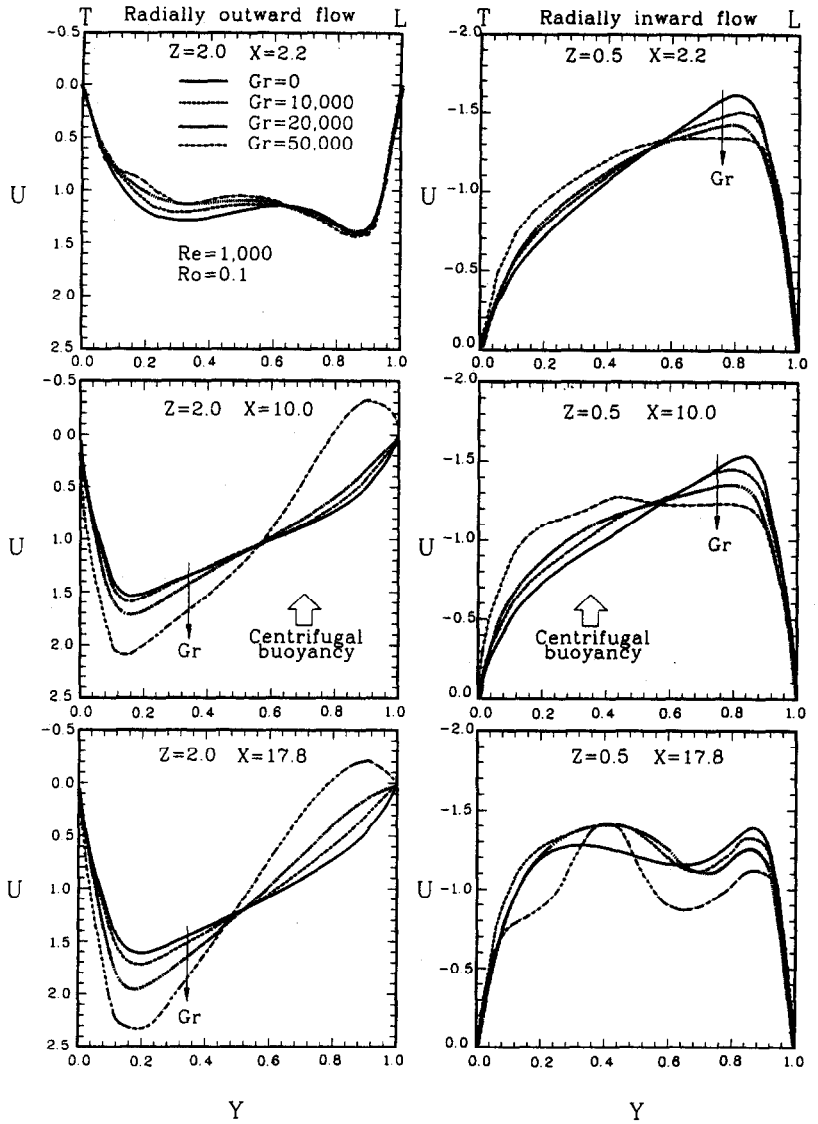

Fig. 4. Effect of centrifugal-buoyancy force on the axial-velocity profiles in the radially inward and outward flow channels, $Re = 1000$ and $Ro = 0.1$.

stantially high values of fluid temperature as well as the temperature gradient are found near the leading wall at channel-middle stations of the radially outward-flow channel. This is because the flow reversal happens in this region, which will accumulate upward the fluid enthalpy from the downstream relatively hot fluids.

Local Nusselt number distribution

Coriolis effect. The effect of Coriolis force on the local Nusselt number distributions along the two-pass channel is depicted in Fig. 6. The rotationally induced buoyancy force and flow Reynolds number are fixed at $Gr = 10{,}000$, and $Re = 500$, respectively; while the rotation number is varied from $Ro = 0.015$ to 0.5. The stationary two-pass square channel, which serves as the reference case for comparison, is also conducted. It is seen from this figure that, at $Ro = 0$, the local Nusselt number distributions along the leading and trailing walls are totally the same. They begin with a local maximum and take a steep fall near the straight entrance due to the renewal of the inlet conditions, then decrease gradually downstream, and then approach to a constant value. This constant value is largely identical to that of the fully developed flow in a stationary straight channel with the constant wall heat flux (center line, [22]). Qualitatively similar trend is also found for the distributions of Nu_x along the right and left side channel walls.

The effect of the rotation induced Coriolis force on the local heat transfer along the orthogonal rotating channel has been described in detail elsewhere [8–14]. Therefore, the present discussion of Fig. 6 lays stress on the comparison of the above-mentioned effects on

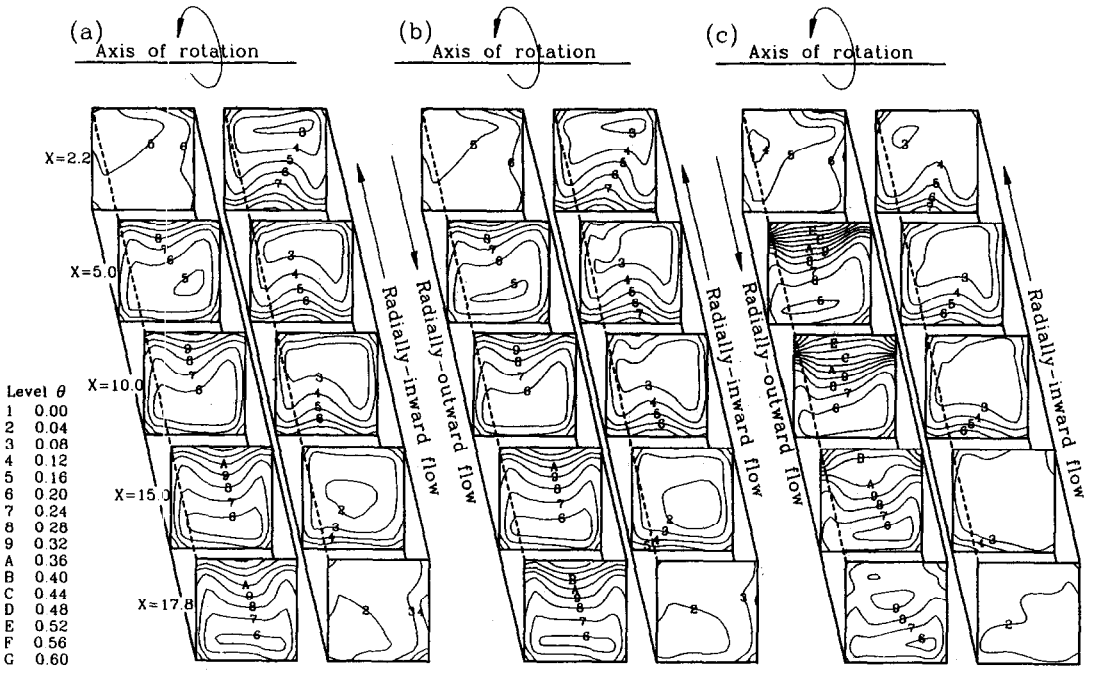

Fig. 5. Development of the isothermal contours along axial distance of the two-pass channel; (a) $Gr = 0$, $Ro = 0$, and $Re = 1000$, (b) $Gr = 10{,}000$, $Ro = 0.1$, and $Re = 1000$, (c) $Gr = 50{,}000$, $Ro = 0.1$, and $Re = 1000$.

the channels of different flow directions. Even then the general tendency of the Coriolis effect is briefly stated below. As given in Fig. 6, the increase in Coriolis force (Ro) yields a significant enhancement in Nu_x on the high-pressure surfaces, moderate increase in Nu_x on the left and right side walls, and slightly degradation in Nu_x on the low-pressure surfaces. With regard to the flow-direction effect, it is seen from this figure that the heat transfer coefficients in the high-pressure surfaces as well as the left and right surfaces are greater for the radially inward flow than those for the radially outward flow at all rotation numbers investigated. Although the magnitude of axial velocity near the high-pressure surfaces for the radially inward flow is sightly smaller than that for the radially outward flow (see Fig. 4, $X = 10$), the cross flow in the radially inward-flow channel is stronger than that for the radially inward-flow channel, which has been shown qualitatively in Fig. 3(b) and (c). Obviously, the combination of these two factors is in favor of the radially inward flow channel. This implies that of the same duct throughflow rate and rotating speed, generally, the assisting buoyancy in the radially inward-flow channel augments the strength of the cross flow, as a result, enhances heat transfer enhancements.

Centrifugal buoyancy effect. Figure 7 shows the effect of centrifugal buoyancy on Nu_x distributions along the four walls of the two-pass channel for $Ro = 0.1$, and $Re = 1000$. The buoyancy force is ranged from $Gr = 10{,}000$ to $50{,}000$. It is seen that the heat transfer on the high-pressure surfaces is increased with increasing the magnitude of buoyancy force for both the radially outward-flow and inward-flow channels. The former is, of course, attributed to the enhanced forced convection through increasing the axial velocity near the trailing wall of the radially outward-flow channel (Fig. 4). As for the radially inward flow, the centrifugal buoyancy slightly decreases the axial velocity near the leading wall, however, in the mean time, it also largely augments the cross-flow intensity (Fig. 3). These two factors compete with each other in their influence on the heat transfer. Evidently, the effect of augmenting the cross-flow intensity overcomes that of the slight decrease in the near-wall velocity. The mechanism of heat transfer augmentation through enhancing the cross-flow intensity is further confirmed by the fact that the heat transfer on the remainding three channel walls of the radially inward-flow channel is slightly enhanced by the centrifugal buoyancy. Attention is now turning to the results of the radially outward flow with the highest Grashof number, $Gr = 50{,}000$ (broad dashed line). Due to the flow reversal near leading wall, the local heat transfer distributions along the four channel walls are bumpy around the region of initiation of flow separation. Significantly poor heat transfer is further found for the low-pressure surface, which is attributed to small axial velocities (Fig. 4) as well as roughly void cross-flow intensities (Fig. 3) near this region.

The relation between the development of the peripherally averaged heat transfer (Nu_x) and that of the

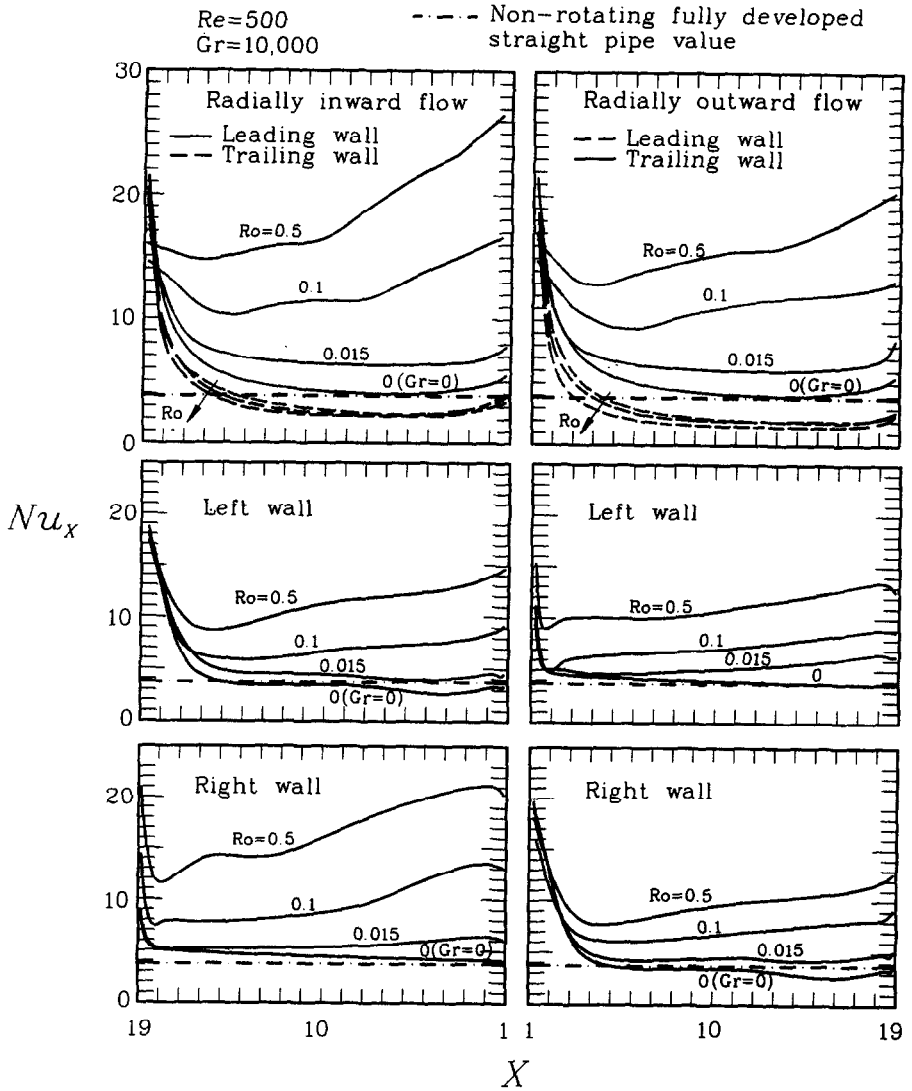

Fig. 6. Effect of rotation number on the local heat transfer in the two-pass channel.

cross-sectionally averaged secondary-flow intensity (σ) is highly interesting and is displayed in Fig. 8. The effect of centrifugal buoyancy on Nu_x and σ is examined. The definition of the cross-flow intensity is given in Nomenclature. It is seen that the centrifugal buoyancy augments significantly the peripherally averaged heat transfer for the co-flowing inward channel, but relatively negligibly for the counter-flowing outward channel. Similar trends are found for the buoyancy-dependence of the development of the secondary-flow intensity in both channels of different flow directions. These encouraging results further quantitatively verify the above explanation of the different mechanisms in heat transfer enhancement between the buoyancy-assisted and buoyancy-against flowing channels.

Comparisons with previous results

Because no data could be found for the rotating channel with a 180° sharp return entrance and exit, the present numerical results are compared with available results of the rotating channels with the uniform (velocity and temperature) inlet conditions, which is given in Fig. 9. The Nusselt number, Nu, is defined as the averaged heat transfer coefficient over the two pass channel from the entrance to exit. it is plotted against $PrReRe_\Omega$. Some theoretical and experimental data superimposed on this figure for comparison include Mori's isothermal-circular-tube correlation [23] and their numerical results for fully developed flows in isothermal or isoflux circular tube [13], Fann and Yang's developing data for isothermal rectangular channel [12], and Hwang and Soong's experimental

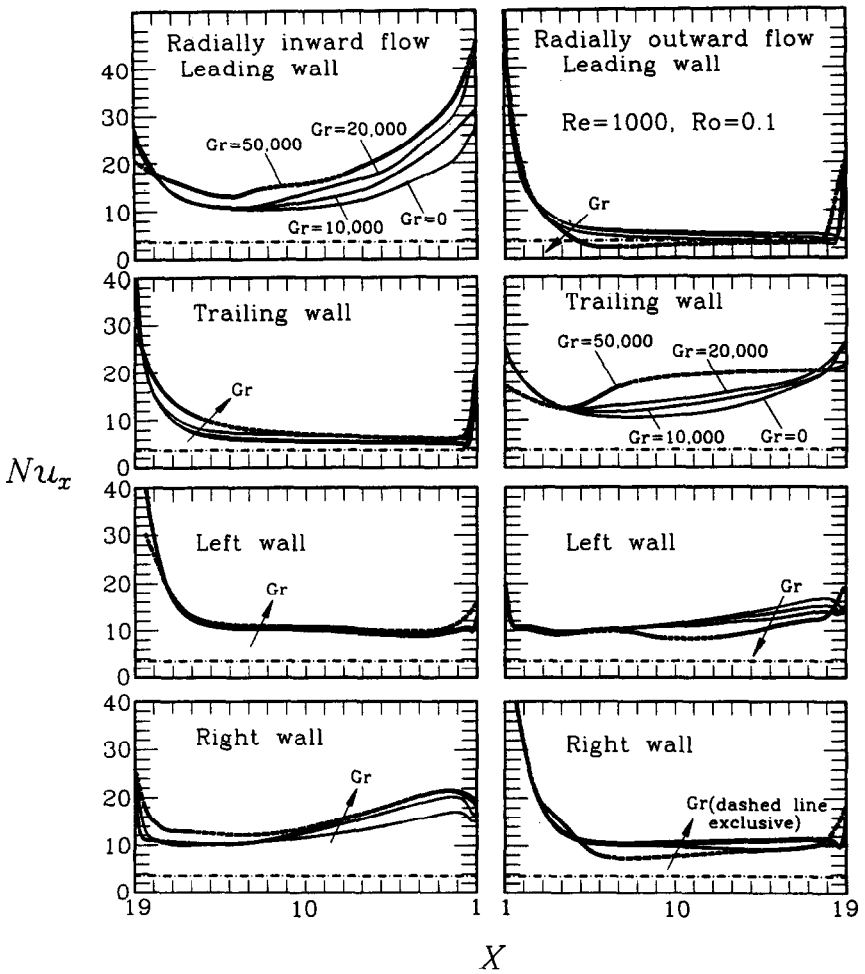

Fig. 7. Effect of Grashof number on the local heat transfer in the two pass channel.

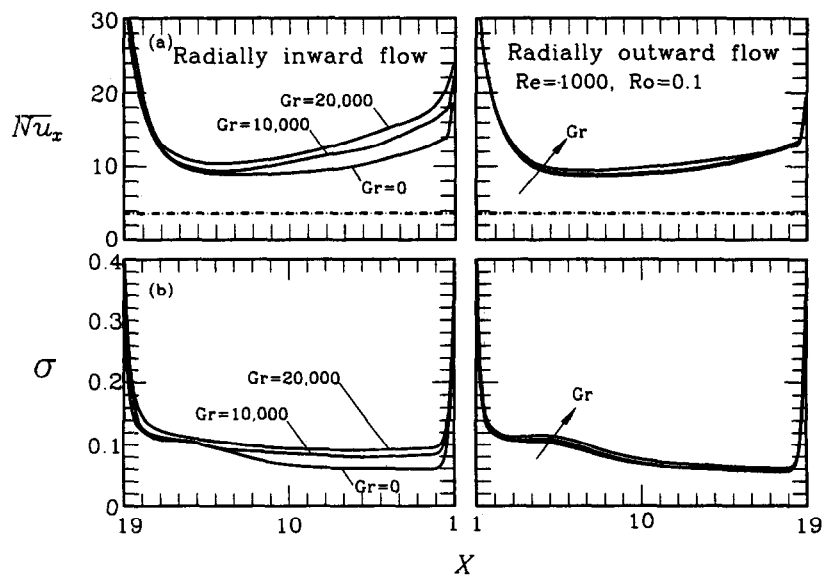

Fig. 8. (a) Effect of rotating buoyancy on the axial variation of the peripherally averaged Nusselt number. (b) Effect of rotating buoyancy on the development of the secondary-flow intensity along the axial distance.

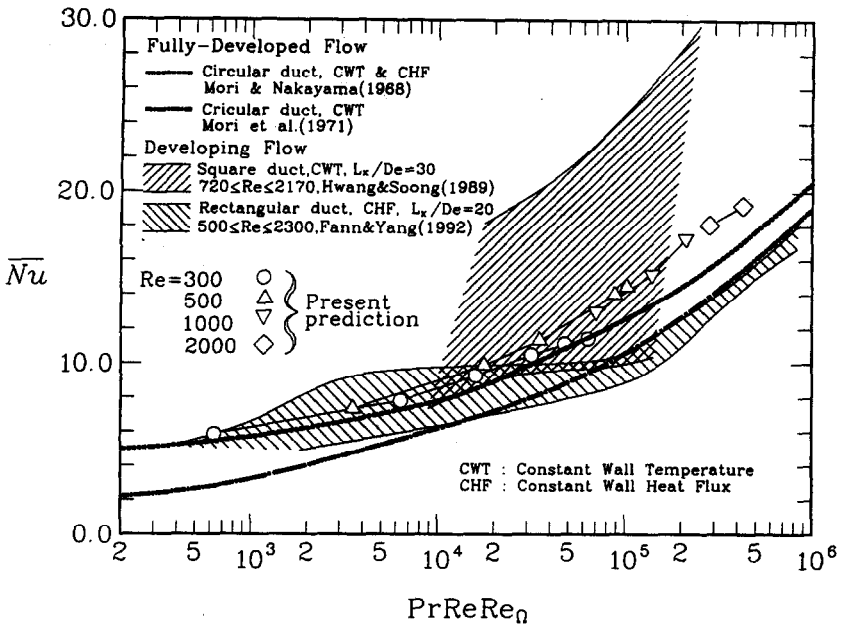

Fig. 9. Comparison of the present predictions of channel-averaged Nusselt number with previous numerical and experimental results.

data [24]. As shown in this figure, the present predictions appear to be slightly higher than those of the empirical correlations [13, 23] and the numerical data [12]. All of them, however, significantly under-predict the measured results [24]. The former is because the present study deals with developing velocity and temperature in relatively shorter channels ($20De$) with a 180° sharp-bend entrance, in which not only the significant entrance effects but also the bend itself result in a higher heat transfer performance. The reason for the latter fact may be attributed to the uncertainties in turbulence level involved in the experiments. Generally speaking, the present predictions have provided satisfactorily reasonable results of two-pass rotating channels.

SUMMARY AND CONCLUSIONS

The equations governing the laminar mixed convection in a periodic two-pass channel with orthogonal rotation have been successfully solved numerically. Owing to the presence of the 180° sharp turn, the numerical calculation of this three-dimensional problem is elliptic in nature. The influences of the rotationally induced Coriolis and centrifugal-buoyancy forces on the heat transfer mechanisms in the radially inward and outward flow channels are investigated. Basically, the Coriolis and centrifugal buoyancy forces affect the heat transfer through altering the axial-velocity distributions as well as the cross-flow patterns. On the basis of the calculated results, the most important features are described as follows:

1. Due to the mechanisms of fluid-thermal interaction, the axial-velocity curves in the radially outward-flow are sharpened by the buoyancy-against effect; while those in the radially inward-flow channel are smoothed off by the buoyancy-assisted effect. In addition, the centrifugal-buoyancy enhances significantly the cross-flow intensity in the radially inward flow, but nearly negligibly in the radially outward flow.
2. Of the same centrifugal buoyancy and duct throughflow rate, the increase in the Coriolis effect (Ro) causes an enhancement in Nu_x on the high-pressure surfaces, a moderate increase in Nu_x on the left and right side surfaces, and a degradation in Nu_x on the low-pressure surfaces of the two-pass channel. This effect is strongly dependent on the flow direction, which is more notable for the buoyancy co-flowing inward channel than for the buoyancy counter-flowing outward channel.
3. Of the same Coriolis force and duct throughflow rate, in general, the centrifugal buoyancy promotes the peripherally averaged heat transfer more significantly in the radially inward-flow channel than in the radially outward-flow channel. This is because the buoyancy-assisted effect augments the heat transfer through enhancing the cross-flow intensity; while only redistribution of the local heat transfer along four channel walls is found for the buoyancy-opposed effect on the radially outward-flow channel.
4. In the radially outward-flow channel, centrifugal buoyancy accelerates the relatively cool fluid near the trailing surface, and decelerates the relatively warm fluid near the leading wall. Whenever the

rotational buoyancy is strong enough, say $Gr = 50{,}000$, the above effects will cause the flow reversal over the leading surface for satisfying the mass conservation, and, as a result, the local heat transfer is significantly reduced in this region.

Acknowledgements—Support for this work was provided by the National Science Council of the Republic of China under contract No. NSC 85-2212-E-216-003.

REFERENCES

1. Cheng, K. C., Shi, L., Kurokana, M. and Chyu, M. K., Visualization of flow patterns in a 180° sharp turn of a square duct. 4th International Symposium on Transport Phenomena and Dynamics of Rotating Machinery. 1988, Honolulu, Hawaii, 541–548.
2. Kajishima, T. and Miyake, Y., Numerical simulation of laminar flow in curved ducts of rectangular cross section. *JSME International Journal*, 1989, **32,** 516–522.
3. Yao, M., Nakatani, M. and Suzuki, K., An experimental study of pressure drop and heat transfer in a duct with a staggered array of cylinders. *Proceedings of ASME-JSME Thermal Engineering Joint Conference*, 1987, **5,** 189–196.
4. Hwang, J. J. and Liou, T. M., Heat transfer and friction in a low-aspect-ratio rectangular channel with staggered perforated ribs on two opposite walls. *Trans. ASME, J. Heat Transfer*, 1995, **117,** 843–850.
5. Hart, J. E., Instability and secondary motion in rotating channel flow. *J. Fluid Mech.*, 1971, **45,** 337–395.
6. Ito, H. and Nanbu, K., Flow in rotating straight pipes of circular cross-section. *Trans. ASME, J. of Basic Eng. Power*, 1972, **94,** 261–270.
7. Spezal, C. G. and Thangam, S., Numerical study of secondary flow and roll-cell instabilities in rotating channel flow. *J. Fluid Mech.*, 1983, **130,** 337–395.
8. Kheshgi, H. S. and Scriven, L. E., Viscous flow through a rotating square channel. *Phys. Fluids*, 1985, **28,** 2968–1979.
9. Hwang, G. J. and Jen, T. C., Convective heat transfer in rotating isothermal ducts. *Int. J. Heat Mass Transfer*, 1990, **33,** 1817–1828.
10. Jen, T. C., Lavine, A. S. and Hwang, G. J., Simultaneously developing laminar convection in rotating isothermal square channels. *Int. J. Heat Mass Transfer*, 1992, **35,** 239–254.
11. Iacovides, H. and Launder, B. E., Parametric and numerical study of fully developed flow and heat transfer in a rotating rectangular duct. *Trans. ASME, J. Turbomachinery*, 1991, **113,** 331–338.
12. Fann, S. and Yang, W. J., Hydrodynamically and thermally developing laminar flow through rotating channels having isothermal walls. *Numerical Heat Mass Transfer*, Part A, 1992, **22,** 257–288.
13. Mori, Y. and Nakayama, W., Convection heat transfer in rotating radial circular pipe (1st report, laminar region). *Int. J. Heat Mass Transfer*, 1968, **11,** 1027–1040.
14. Wagner, J. H., Johnson, B. V. and Hajek, T. J., Heat transfer in rotating passages with square smooth walls and radial outward flow. *Trans. ASME, J. Turbomachinery*, 1991, **113,** 42–51.
15. Wagner, J. H., Johnson, B. V. and Kopper, F. C., Heat transfer in rotating serpentine passages with smooth walls. *Trans. ASME, J. Turbomachinery*, 1991, **113,** 321–330.
16. Wagner, J. H., Johnson, B. V., Grazinani, R. A. and Yeh, F. C., Heat transfer in rotating serpentine passages with trips normal to the flow. *Trans. ASME, J. Turbomachinery*, 1992, **114,** 847–857.
17. Yang, W. J., Zhang, N. and Chiou, J., Local heat transfer in a rotating serpentine flow passage. *Trans. ASME, J. Heat Transfer*, 1992, **114,** 354–361.
18. Patankar, S. V., Liu, L. H. and Sparrow, E. M., Fully developed flow and heat transfer ducts having periodic variations of the cross-sectional area. *Trans. ASME, J. Heat Transfer*, 1977, **99,** 180–186.
19. Patankar, S. V., *Numerical Heat Transfer and Fluid Flow*, Hemisphere, Washington, DC, 1980.
20. Van Doormaal, J. P. and Raithby, G. D., Enhancements of the SIMPLE method for predicting incompressible fluid flows. *Numerical Heat Mass Transfer*, Part A, 1992, **7,** 147–163.
21. Liou, T. M., Hwang, J. J. and Chen, S. H., Simulation and measurement of enhanced turbulent heat transfer in a channel with periodic rib on one principal wall. *Int. J. Heat Mass Transfer*, 1992, **38,** 3194–3207.
22. Kays, W. and Crawford, M., *Convective Heat and Mass Transfer*, McGraw-Hill, New York, 1980.
23. Mori, Y., Fudaka, T. and Nakayama, W., Convective heat transfer in rotating circular pipes. *Int. J. Heat Mass Transfer*, 1971, **14,** 1807–1824.
24. Hwang, G. J. and Soong, C. Y., Experimental automation and heat transfer measurement on a rotating thermal system. *Transport Phenomena in Thermal Control*, 375–388, Hemisphere, New York, 1989.